Structural, vibrational, and electrical transport properties of nodal-line semimetal candidate CaCdGe under high pressure

Xiaolan Du,[1] Chao An,[1,2,*] Xuliang Chen,[3] Ying Zhou,[1] Min Zhang,[1] Shuyang Wang,[3] Chunhua Chen,[3] Yonghui Zhou,[3] Xiaoping Yang,[3,4] and Zhaorong Yang[1,3,4,†]

[1]*Information Materials and Intelligent Sensing Laboratory of Anhui Province, Institutes of Physical Science and Information Technology, Anhui University, Hefei 230601, China*

[2]*Key Laboratory of Structure and Functional Regulation of Hybrid Materials (Anhui, University), Ministry of Education, Hefei 230601, China*

[3]*Anhui Province Key Laboratory of Condensed Matter Physics at Extreme Conditions, High Magnetic Field Laboratory, Chinese Academy of Sciences, Hefei 230031, China*

[4]*High Magnetic Field Laboratory of Anhui Province, Hefei 230031, China*

(Received 22 February 2023; revised 5 June 2023; accepted 12 July 2023; published 24 July 2023)

Nodal-line semimetals provide the opportunity to explore exotic properties owing to their nontrivial band structures. Here, the structural and electronic properties of nodal-line semimetal candidate CaCdGe were systematically investigated under pressure up to 53.3 GPa through synchrotron x-ray diffraction, Raman scattering, electrical transport measurements, and theoretical calculations. Upon compression, although no trace of evident structural transition is detected, a maximum value of lattice ratio c/a and abnormal changes in bond angles around $P_C \sim 12.5$ GPa are observed from our x-ray diffraction data. Meanwhile, a new Raman peak is observed in the vicinity of P_C. Furthermore, the resistance parameters (n, A, and Θ_R) all show the abrupt changes above P_C. Since the electronic topological transition is absent within 30.0 GPa based on band structure calculations, our results may demonstrate the occurrence of a subtle isostructural transition around P_C in pressurized CaCdGe, due to the distortion of $CdGe_4$ tetrahedra.

DOI: 10.1103/PhysRevB.108.014109

I. INTRODUCTION

Topological nodal-line semimetals (NLSMs), classified into a new type of topological material in addition to the Dirac/Weyl semimetals, have recently attracted wide research interests due to their topological nontrivial electronic states [1–5]. The nodal line is formed by the intersection of linearly dispersive bands along a one-dimensional line in the three-dimensional Brillouin zone [3]. Accordingly, various interesting properties, such as drumhead surface states [5], high carrier mobility [2], and extremely large magnetoresistance (MR) [6,7] are realized unique to the nodal line. Up to now, many materials are predicated to be the topological NLSM, such as ZrSiS [1], $PbTaSe_2$ [8], CaP_3 [9], and $SrAs_3$ [10]. Based on previous studies, the physical properties of NLSMs can be effectively tuned through applying external parameters. For instance, the Fermi surface of ZrSiS undergoes a Lifshitz transition under a uniaxial tensile stress [11]. Upon compression, topological quantum phase transitions are reported in both $PbTaSe_2$ [12] and ZrSiS [13]. Moreover, superconductivity is induced in the pressurized $SrAs_3$ [14,15].

Recently, ternary hexagonal compounds CaTX (T = Ag, Cd; X = As, P, Ge) were proposed as a new family of NLSM candidates [6,16–22]. They crystallize in the $P\bar{6}2m$ space group (No. 189), which contain mirror reflection symmetry but have no inversion symmetry [20,22–24]. The nodal-line structures were initially predicted in CaAgP and CaAgAs by first-principles calculations [21,22]. Subsequently, the topological nontrivial states of this system were further verified through various experimental measurements [6,17,18,20,23,24]. For example, the extremely large MR with clear Shubnikov–de Haas (SdH) oscillations was observed in CaCdGe [6]. The nontrivial phases of CaAgAs were revealed via de Haas–van Alphen oscillations [17,18]. In addition, its topological surface appearing as a circular hole pocket was further uncovered by angle-resolved photoemission spectroscopy (ARPES) [20,23,24]. When bulk CaAgAs is reduced to the thin film, the feature of topological surface state can be more clearly probed, which manifests as a steep increase of MR at low magnetic field due to the weak antilocalization effect [25]. Recently, combined with ARPES measurements and theoretical calculations, a topological quantum phase transition in $CaAg(P_{1-x}As_x)$ was revealed with partial As substitution [19]. In addition, the superconductivity with T_C = 1.7–1.8 K was further realized in the Pd-doped CaAgP single crystal [16]. Based on the above studies, the electronic properties of the CaTX system can be highly tuned via chemical doping; however, additional defects and impurities are inevitably introduced [16,19], thus a clean tuning tool, in particular, is required.

Pressure, as a thermodynamic variable, is an effective and clean way to modulate the lattice as well as electronic states

*Corresponding author: chaoan@ahu.edu.cn
†Corresponding author: zryang@issp.ac.cn

[26–28]. Here, we choose NLSM candidate CaCdGe and systematically investigate its structural and electronic properties under high pressure. With increasing pressure up to 48.5 GPa, no trace of evident structural transition is detected based on our x-ray diffraction (XRD) data. However, anomalies in lattice ratio *c*/*a* and bond angles are observed around $P_C = 12.5$ GPa. In addition, a new peak in Raman spectra is observed across 9.5 GPa. Moreover, the resistance parameters all exhibit the huge changes above 13.7 GPa. Considering the absence of electronic topological transition based on our theoretical calculations, all the above experimental results may indicate the occurrence of a pressure-induced subtle isostructural transition around P_C in CaCdGe.

II. EXPERIMENTAL AND CALCULATION METHODS

CaCdGe single crystals were grown by Cd self-flux method [6]. The high quality of as-grown single crystals was checked by x-ray diffraction and energy-dispersive x-ray spectra. The electrical resistance and magnetoresistance at ambient pressure were conducted with the standard four-probe method in a physical property measurements system (Quantum Design, Inc.)

High-pressure electrical transport measurements were conducted in a standard Be-Cu alloy diamond-anvil cell (DAC) made by the Honest Machinery Designer Corporation, Japan. The diameter of the diamond culet is 300 μm. A T301 stainless-steel gasket was preindented from a thickness of 200 to 30 μm, leaving a pit inside the gasket. A hole with a diameter of 285 μm was drilled at the center of the pit using laser ablation. The indented gasket was then covered with a mixture of epoxy and fine cubic boron nitride (cBN) powder and compressed firmly to insulate the electrode leads from the metallic gasket. A hole with a diameter of 100 μm was further drilled at the center of the cBN-covered pit. Soft NaCl fine powder was used as the pressure-transmitting medium (PTM). A piece of cleaved single crystal with size of $\sim 80 \times 50 \times 10\ \mu m^3$ together with some ruby powders was loaded into the chamber. The sample was forced to contact with four Pt foils in a standard four-probe configuration.

High-pressure powder x-ray diffraction experiments were conducted at beamline 15U1, Shanghai Synchrotron Radiation Facility at room temperature [29]. Pressure was generated by a Mao-Bell type symmetric DAC. The culet of the diamond was 300 μm in diameter. The rhenium gasket was preindented from a thickness of 200 to 30 μm and a hole with a diameter of 150 μm was drilled as a sample chamber. CaCdGe powders were obtained by crushing and grinding the as-prepared CaCdGe single crystals. Daphne 7373 oil was used as the PTM. A focused monochromatic x-ray beam with wavelength 0.6199 Å was used for the angle-dispersive diffraction. The size of the focused x-ray beam at the sample position is 3 μm × 2.5 μm. Two-dimensional area detector Mar165 CCD was used to collect the powder diffraction patterns. The detector was 185.88 mm away from the sample. The DIOPTAS [30] and GSAS programs [31] were employed for image integrations and structural refinement, respectively.

Raman-scattering measurements were performed at room temperature on freshly cleaved CaCdGe single crystals using a commercial Renishaw spectroscopy system with a 532-nm laser line in backscattering configurations. The excited laser power was kept at 0.5 mW to avoid sample damage and any heating effect. The laser beam was focused on the sample by a 20× objective. The polarized Raman spectra at ambient temperature and pressure were measured with the polarization of the scattered photons (E_s) parallel to that of the incident photons (E_i), i.e., $E_i \parallel E_s$. In addition, the laser propagation direction is parallel to the *a* axis [see Fig. 1(c)]. The high-pressure Raman spectra were performed at room temperature in a Mao-Bell type symmetric DAC. The diameter of the diamond culet is 300 μm. The T301 stainless-steel gasket was preindented from a thickness of 200 to 30 μm and a hole of about 150 μm was drilled as the sample chamber. Argon (run 1) and Daphne 7373 oil (run 2) served as the PTM, respectively. Pressure was calibrated by using the ruby fluorescence shift at room temperature for all the above experiments [32].

The phonon vibrational frequency at the Γ point was investigated by using the frozen-phonon method, which constructs the force-constant matrix by a small-displacement method in the harmonic approximation [33]. The geometry structure was fully optimized before performing force constants calculation, by using the Vienna *Ab initio* simulation package (VASP) [34,35] within the framework of generalized gradient approximation (Perdew-Burke-Ernzerhof exchange functional) [36]. The ion-electron interaction was modeled by the projector augmented wave method [37,38] with a uniform energy cutoff of 400 eV. Spacing between *k* points was 0.015 $Å^{-1}$. Finally, the optimal structure was obtained when the residue forces acting on all the atoms were less than 0.001 eV/Å. For an accurate band structure description, spin-orbit coupling effect and the modified Becke-Johnson [39] exchange-correlation potential were further introduced.

III. RESULTS AND DISCUSSION

CaCdGe crystallizes in a ZrNiAl-type structure with space group $P\bar{6}2m$ (No. 189) [Fig. 1(a)], where $CdGe_4$ tetrahedra form a three-dimensional kagome triangular lattice while Ca atoms are located at the shared edges and corners [6]. There are totally nine atoms (three Ca, three Cd, and three Ge) in a unit cell. Figure 1(b) shows a typical XRD pattern of CaCdGe single crystal ($\lambda = 1.54184$ Å). The observation of only (*h*00) reflections indicates that the *bc* plane is a natural cleavage facet of the crystals. The upper right inset shows the photo image of CaCdGe single crystals. The powder XRD pattern is displayed in Fig. 1(c). The impurity peak is marked by a star, which is ascribed to the fluxing medium Cd. The refined lattice parameters are $a = 7.313(4)$ and $c = 4.488(2)$ Å, which are close to the values in the previous report [6]. The energy-dispersive x-ray spectra with point and area-scanning modes give the ratio of Ca:Cd:Ge as 1:1.003:0.997 [see Fig. 1(d)]. Figure 1(e) shows the temperature dependence of resistance of CaCdGe single crystal. The current is introduced along the *bc* plane. The resistance monotonically decreases upon cooling the temperature, exhibiting a typical metallic conduction behavior [6]. In addition, the MR of CaCdGe is measured at different temperatures with external magnetic field perpendicular to the *bc* plane. Clear SdH oscillations are observed, as shown in the inset of Fig. 1(f). After using a fast Fourier transform analysis, a prominent frequency labeled

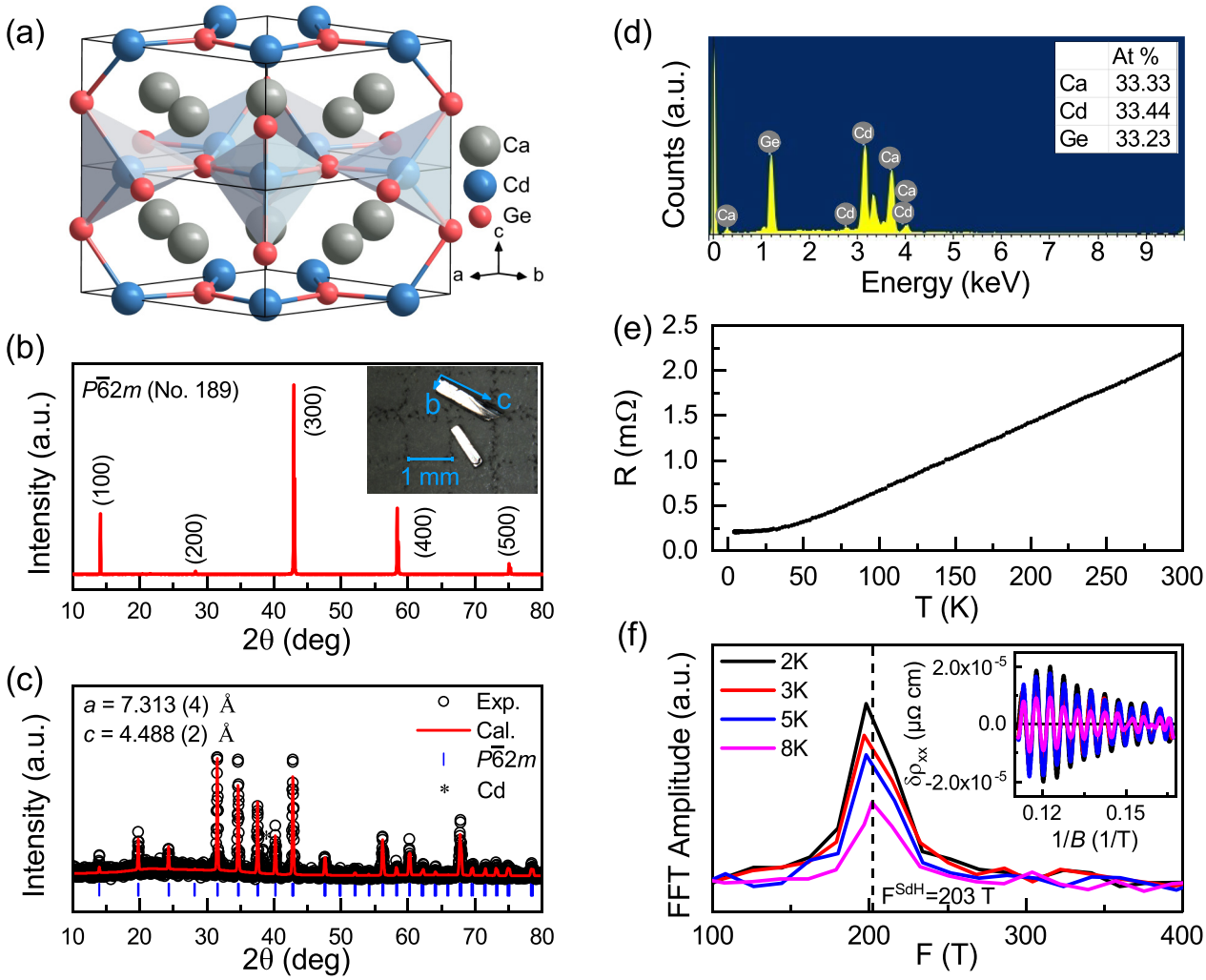

FIG. 1. (a) Lattice structure of CaCdGe. (b) XRD pattern of CaCdGe single crystal. The inset shows the photo of as-grown CaCdGe single crystal. (c) The powder XRD pattern of CaCdGe. Lattice parameters (a and c) are extracted through structural refinements. The star stands for the Cd impurity. (d) Energy-dispersive x-ray spectroscopy of CaCdGe single crystal. (e) Temperature dependence of resistance of CaCdGe single crystal. (f) Temperature dependence of the fast Fourier transformed Shubnikov–de Haas (SdH) data. Inset: SdH oscillations part, $\delta\rho_{xx}$, as a function of $1/B$ at various temperatures.

as $F^{\mathrm{SdH}} = 203\,\mathrm{T}$ is detected, in excellent accordance with previous study [6]. All the above experimental results show the high quality of our as-grown CaCdGe single crystals.

We first investigated the structural symmetry of CaCdGe under high pressure. The high-pressure XRD patterns of CaCdGe at room temperature are displayed in Fig. 2. With increasing pressure, all Bragg peaks move to higher angles due to the shrinkage of the lattice without the appearance of new peaks up to the highest pressure of 48.5 GPa [see Fig. 2(a)]. The XRD pattern at each pressure can be well indexed by the space group $P\bar{6}2m$ [see the representative refinements at 0.5 and 48.5 GPa in Figs. 2(b) and 2(c)]. The extracted lattice parameters (a and c) are displayed in Fig. 2(d). Without detecting an evident structural transition, it can be seen that lattice parameters decrease smoothly upon compression. Moreover, the unit cell volume as a function of pressure is shown in Fig. 2(e), which is fitted by using the third-order Birch-Murnaghan equation of state [red dashed line in Fig. 2(e)] [40]: $P = \frac{3}{2}B_0[(\frac{V_0}{V})^{7/3} - (\frac{V_0}{V})^{5/3}]\{1 + \frac{3}{4}(B'_0 - 4)[(\frac{V_0}{V})^{2/3} - 1]\}$, where V_0, B_0, and B'_0 are the volume, bulk modulus $V/(dV/dP)$, and first-order derivative of the bulk modulus at zero pressure, respectively. The fitting yields $V_0 = 207.4(\pm 2.0)\,\mathrm{Å}^3$, $B_0 = 73.1(\pm 10.1)\,\mathrm{GPa}$, and $B'_0 = 4.2(\pm 0.6)$.

We further plot the lattice ratio c/a, bond lengths, and bond angles as a function of pressure, as shown in Fig. 3. It can be seen that the $CdGe_4$ tetrahedra contains two different sites of Ge atoms, i.e., Ge1 and Ge2 [see Fig. 3(a)], thus forming two covalent bonds (Cd1-Ge1 and Cd1-Ge2). With increasing pressure, both bond lengths ($d_{\mathrm{Cd1\text{-}Ge1}}$ and $d_{\mathrm{Cd1\text{-}Ge2}}$) decrease smoothly while bond angles ($\angle$Ge1-Cd1-Ge1 and $\angle$Ge1-Cd1-Ge2) show abrupt changes above $P_C \sim 12.5\,\mathrm{GPa}$. Meanwhile, a maximum of lattice ratio c/a is observed around P_C [see Fig. 3(d)]. Since no evident structural transition takes place under pressure, these changes in lattice compression behavior are indicative of an isostructural transition [41–43]. The detailed analysis will be discussed latter.

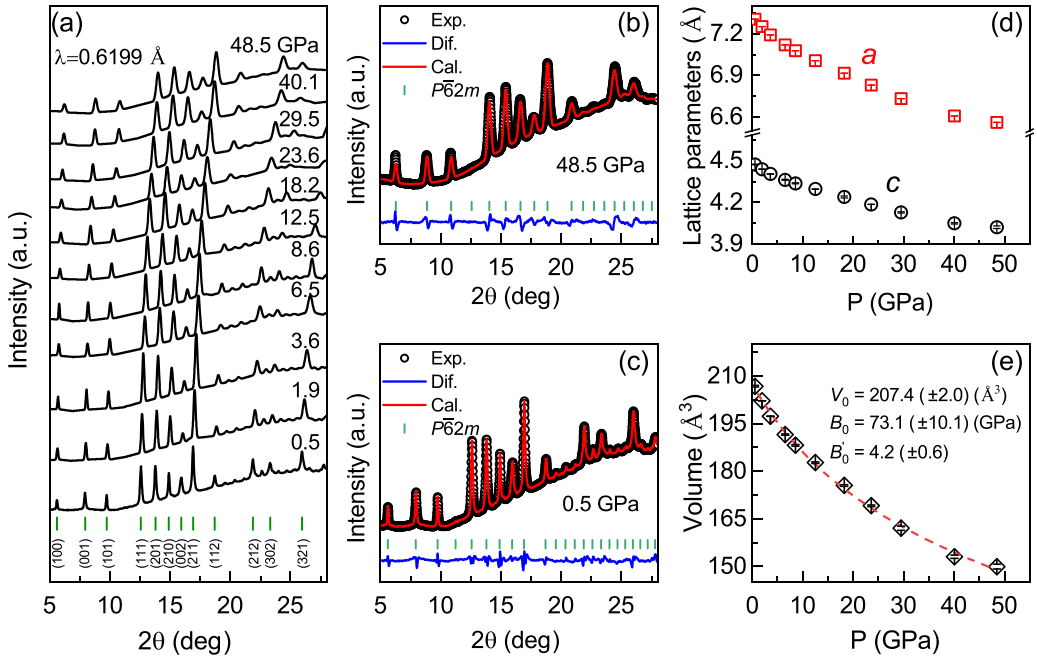

FIG. 2. (a) Synchrotron radiation x-ray diffraction patterns of CaCdGe under various pressures ($\lambda = 0.6199$ Å). (b),(c) The structural refinements at 0.5 and 48.5 GPa were performed by using the standard Rietveld method. The open circles and red line represent the observed and calculated data, respectively. The vertical bars indicate the position of Bragg peaks. (d) Pressure-dependent lattice parameters (a and c). (e) Volume as a function of pressure. The open symbols stand for unit volume. The red dashed line is the fitting result based on the third-order Birch-Murnaghan equation of states.

Raman scattering has been proven to be a powerful and effective tool in probing the lattice vibrations, which is sensitive to the local lattice symmetry and can provide information including electron-phonon coupling, weak lattice distortion, and structural transition [44–46]. Figure 4(a) shows the room temperature Raman spectrum of CaCdGe single crystal. At first glance, six Raman peaks are clearly observed in the range of 50–210 cm^{-1}. To figure out the specific Raman vibrational mode of these peaks, polarized Raman spectra are measured with polarization of the incident photons (E_i) parallel to that of the scattered photons (E_s), i.e., $E_i \parallel E_s$, as shown in Fig. 4(b). It can be seen that five high-frequency peaks show twofold symmetry while the lowest-frequency peak shows fourfold symmetry. According to the theoretical calculations, CaCdGe has the point group D_{3h} and its irreducible representations at the Γ point are

$$\Gamma_{\text{acoustic}} = E' \oplus A_2'';$$

$$\Gamma_{\text{optic}} = 6E' \oplus 2E'' \oplus 3A_2'' \oplus 2A_2' \oplus A_1'' \oplus 2A_1'$$

Among these irreducible representations, A_1' and E'' modes are Raman active; the A_2'' mode is IR active. In particular, the E' mode is both Raman and IR active. Considering that E' and E'' modes are both double-degenerate modes, thus there are totally 20 ($7E' \oplus 2E'' \oplus 2A_1'$) Raman vibrational modes and 18 ($7E' \oplus 4A_2''$) IR vibrational modes. In addition, the intensity of polarized Raman peaks is proportional to $|\hat{e}_i \cdot R \cdot \hat{e}_s|^2$, where $\hat{e}_i$ and $\hat{e}_s$ are the polarization unit vector of the incident and scattered light, respectively, and R is the Raman tensor. The Raman tensors of the Raman-active modes are written as

$$A_1' = \begin{pmatrix} a & 0 & 0 \\ 0 & a & 0 \\ 0 & 0 & b \end{pmatrix}; \quad E' = \begin{pmatrix} 0 & 0 & 0 \\ 0 & 0 & c \\ 0 & c & 0 \end{pmatrix};$$

$$E'' = \begin{pmatrix} 0 & 0 & -c \\ 0 & 0 & 0 \\ -c & 0 & 0 \end{pmatrix};$$

$$E'(x) = \begin{pmatrix} d & 0 & 0 \\ 0 & -d & 0 \\ 0 & 0 & 0 \end{pmatrix} \quad \text{and}$$

$$E'(y) = \begin{pmatrix} 0 & -d & 0 \\ -d & 0 & 0 \\ 0 & 0 & 0 \end{pmatrix}.$$

Here, we define θ as the angle between the c axis and E_i. Since the polarization of the incident photons is parallel to that of the scattered photons (i.e., $E_i \parallel E_s$) and the laser propagation direction is parallel to the a axis, thus the Raman intensity is given by

$$A_1': \quad \text{Intensity} = (a\sin^2\theta + b\cos^2\theta)^2, \tag{1}$$

$$E'': \quad \text{Intensity} = (c\sin 2\theta)^2 \text{ or } 0, \tag{2}$$

$$E'(x): \quad \text{Intensity} = (d\sin^2\theta)^2, \tag{3}$$

$$E'(y): \quad \text{Intensity} = 0. \tag{4}$$

Based on Eqs. (1)–(4), we know that A_1', E'', and E' Raman modes can be experimentally observed under the configuration of $E_i \parallel E_s$. With increasing angle (θ), the intensities of

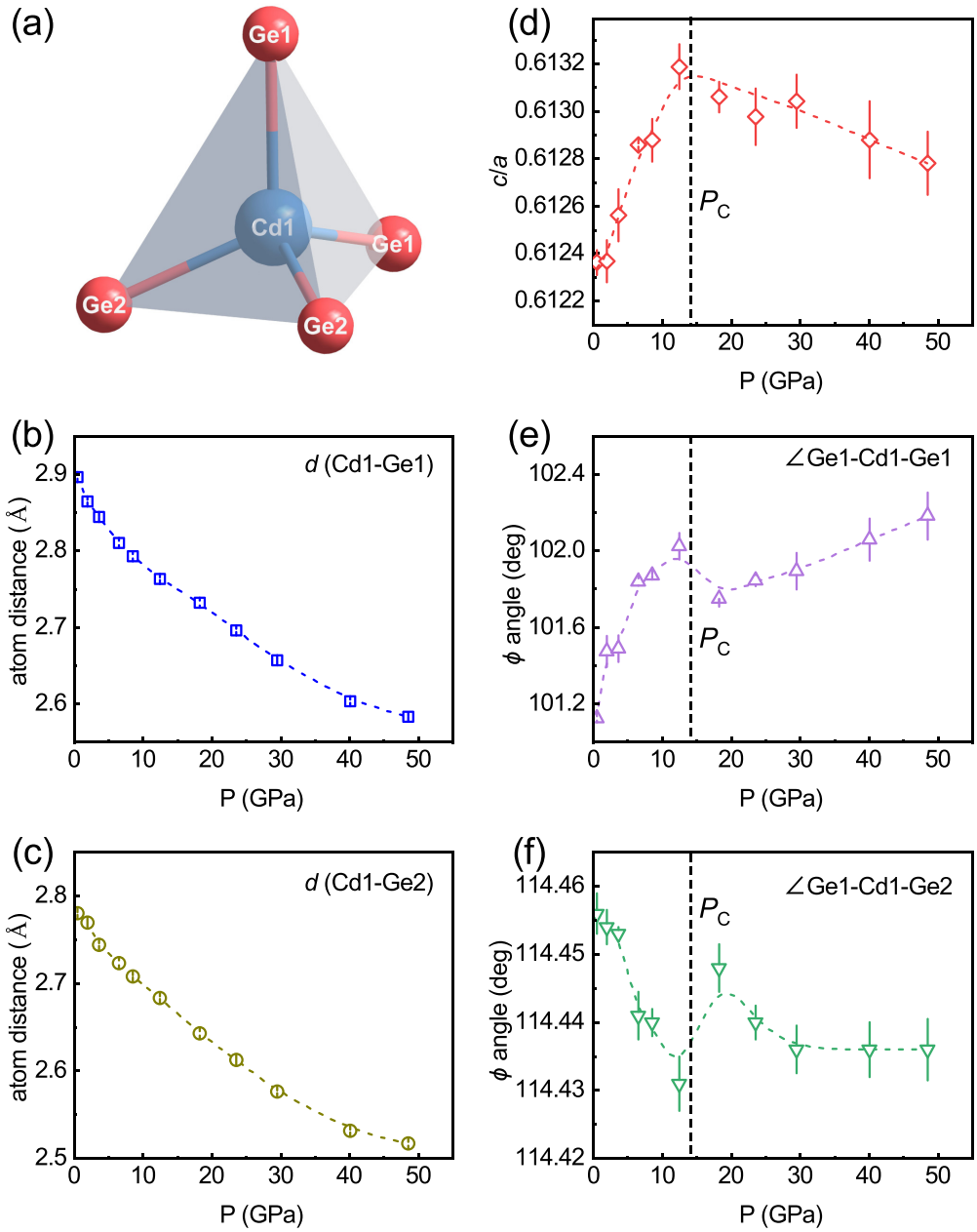

FIG. 3. (a) An illustration of the $CdGe_4$ tetrahedra. (b),(c) Pressure dependence of $d_{Cd1\text{-}Ge1}$ and $d_{Cd1\text{-}Ge2}$. (d) Lattice ratio c/a as a function of pressure. (e),(f) Pressure dependence of the Ge1-Cd1-Ge1 and Ge1-Cd1-Ge2 bond angles in the tetrahedral coordination. The vertical dashed lines represent the critical pressure.

both A_1' and E' modes exhibit twofold symmetry while that of the E'' mode exhibits fourfold symmetry. Therefore, the lowest-frequency Raman peak with fourfold symmetry can be assigned to the E'' vibrational mode while other peaks are assigned to the A_1' or E' modes [see Fig. 3(a)]. Here, the Raman spectrum is further fitted by using the Lorentzian line shape. However, we find that the peaks around 175 cm^{-1} could be well fitted by three Lorentzian lines. Combined with the theoretical calculation results, we demonstrate that these peaks actually consist of E'-2, A_1'-2, and E'-3 Raman vibrational modes. Therefore, totally seven Raman peaks located at 80.8 (E''), 112.5 (A_1'-1), 130.6 (E'-1), 172.7 (E'-2), 175.5 (A_1'-2), 180.7 (E'-3), and 202.1 (E'-4) cm^{-1} are determined at ambient pressure. The detailed information of Raman vibrational modes based on theoretical calculations and experimental results are summarized in Table I.

Now, we focus on the pressure effect on these Raman modes. Figure 5(a) shows the room temperature Raman spectra of CaCdGe single crystal under high pressure up to 16.3 GPa with argon as the PTM (run 1). At 1.3 GPa, seven Raman peaks are determined: one E'' mode, two A_1' modes and four E' modes [see Fig. 5(b)]. With initial increasing pressure, all Raman modes monotonically shift to higher wave numbers (blueshift), indicating the overall shrinkage of the crystal lattice. In addition, the A_1'-2 mode is gradually visible at 3.8 GPa and becomes more and more evident. More importantly, upon further compression to 9.7 GPa, a new peak (labeled as Q) around 154.3 cm^{-1} appears, marked as

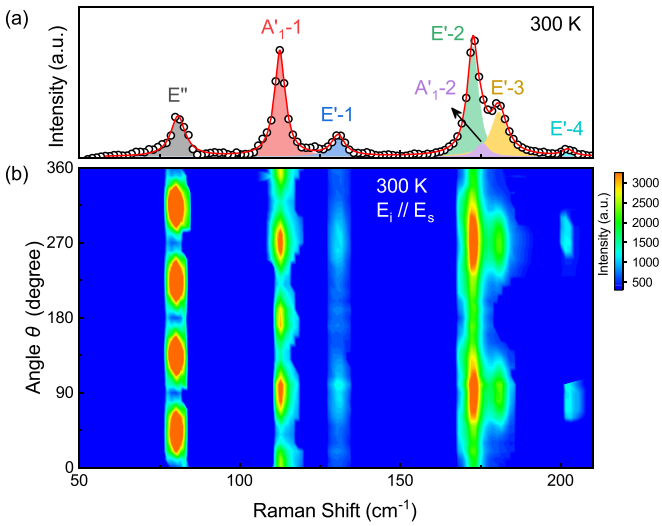

FIG. 4. (a) Room temperature Raman spectrum of cleaved CaCdGe single crystal. (b) Polarized Raman spectra of CaCdGe single crystal at room temperature with the polarization of incident photons (E_i) parallel to that of the scattered photons (E_s), i.e., $E_i \parallel E_s$.

a star in Fig. 5(a). After releasing the pressure back to 0 GPa, the Raman peaks return to the original profile, indicating the evolution of Raman modes upon compression is reversible. We have further conducted high-pressure Raman experiment using Daphne 7373 oil as the PTM up to 52.9 GPa (run 2), as shown in Fig. 5(c). Similar to run 1, the same seven Raman modes are determined at 1.0 GPa [Fig. 5(d)]. Meanwhile, a new peak marked as a star around 153.0 cm^{-1} is observed at 9.5 GPa, which is reproducible compared with run 1 except for a minor difference in the critical pressure value. Lorentzian line-shape fitting of Raman spectra at selected pressures for two runs are displayed in Fig. S1 (Supplemental Material [47]). To obtain a clear view, the peak positions of Raman modes as a function of pressure are displayed in Fig. 5(e). It can be seen that both experiments (run 1 and run 2) show the appearance of the new Raman peak Q upon compression. It can also be tracked in the contour plot of Raman spectra, as shown in Fig. 5(f). In addition, there are some differences between these two Raman-scattering experiments. First, the

TABLE I. Comparison between theoretical calculation and experimental results of CaCdGe Raman vibrational modes at ambient pressure.

No.	Symmetry	Vibrational orientation	Calculation (0 K) (cm^{-1})	Experiment (300 K) (cm^{-1})
1	E'	*ab*	75.3	
2	E''	*c*	78.1	80.8
3	A_1'	*ab*	108.3	112.5
4	E'	*ab*	122.9	
5	E'	*ab*	124.7	130.6
6	E''	*c*	156.4	
7	E'	*ab*	162.9	172.7
8	A_1'	*ab*	163.6	175.5
9	E'	*ab*	170.1	180.7
10	E'	*ab*	188.3	202.1

A_1'-2 mode is clearly visible at 3.8 GPa in run 1 while that just can be observed above 9.5 GPa in run 2. Second, the E'-4 mode is always observed in run 1 while it seriously broadens and is hardly tracked in run 2. Third, the full width at half maxima (FWHM) of Raman modes broaden more evidently in run 2 upon compression, especially for the A_1'-2 mode (see Fig. S2, Supplemental Material [47]). Here, all these discrepancies between two runs could be related to the presence of deviatoric stress under high pressure since Daphne 7373 oil is used as the PTM [48].

In principle, the appearance of new Raman peaks upon compression usually involves a crystal symmetry breaking [49–51]. However, since there is no trace of evident structural transition under pressure based on our XRD data, the new Raman peak Q observed here should be attributed to the other origin. On one hand, we note that in many previous reports without evident structural transitions, the appearance of new Raman peaks in high-pressure Raman spectra have been usually considered as experimental signatures of a pressure-induced isostructural transition [52–55]. This isostructural transition does not show any new Bragg peaks in XRD pattern but involves subtle changes in lattice, such as tilt and rotation of the polyhedra [54–56], and discontinuity in bond lengths and angles [42,53,55].

On the other hand, the above abnormal behaviors in Raman and XRD data can also be driven by an electronic topological transition (ETT). An ETT occurs when a band extremum, which is associated to a Van Hove singularity, crosses the Fermi level (E_F) and leads to a strong redistribution of the electronic density of states (EDOS) near E_F [57]. This EDOS redistribution can lead to anomalies in Raman spectra as well as the lattice compressibility [58–61]. In particular, similar behaviors are reported in many high-pressure studies of topological electronic materials, such as Bi_2Se_3 [59], Bi_2Te_3 [62,63], Sb_2Se_3 [61], and Sb_2Te_3 [64]. Here, the maximum of lattice ratio *c*/*a* and the appearance of a new Raman peak Q are observed in our present work. According to the group theory, the E' vibrational mode of CaCdGe is a double-degenerate mode, which may be lifted in the vicinity of ETT [65] and thus resulting in the appearance of a new Raman peak above 9.5 GPa. In order to further confirm whether the ETT takes place, the band structures of CaCdGe are calculated under pressure, as shown in Fig. S3 (Supplemental Material [47]). With increasing pressure up to 30.0 GPa, the electronic pocket at the *K* point is monotonically lifted while the hole pocket around the Γ point moves downwards a bit. Nevertheless, the band structure of CaCdGe maintains its original feature upon compression, i.e., both energy bands (located around the *K* and Γ points) cross the Fermi level, which evidences the absence of ETT. In addition, recalling that the bond angles of $CdGe_4$ tetrahedra show the abrupt changes above P_C, these anomalous behaviors in our case are most likely attributed to a subtle isostructural transition, due to the distortion of $CdGe_4$ tetrahedra upon compression. It is worth noting that the discrepancy in the critical pressure (9.5 GPa for Raman; 12.5 GPa for XRD) could be attributed to different sensitivity of these two methods.

Furthermore, we have conducted electrical transport measurements of CaCdGe single crystal under high pressure, as shown in Fig. 6. At 3.9 GPa, the temperature dependence

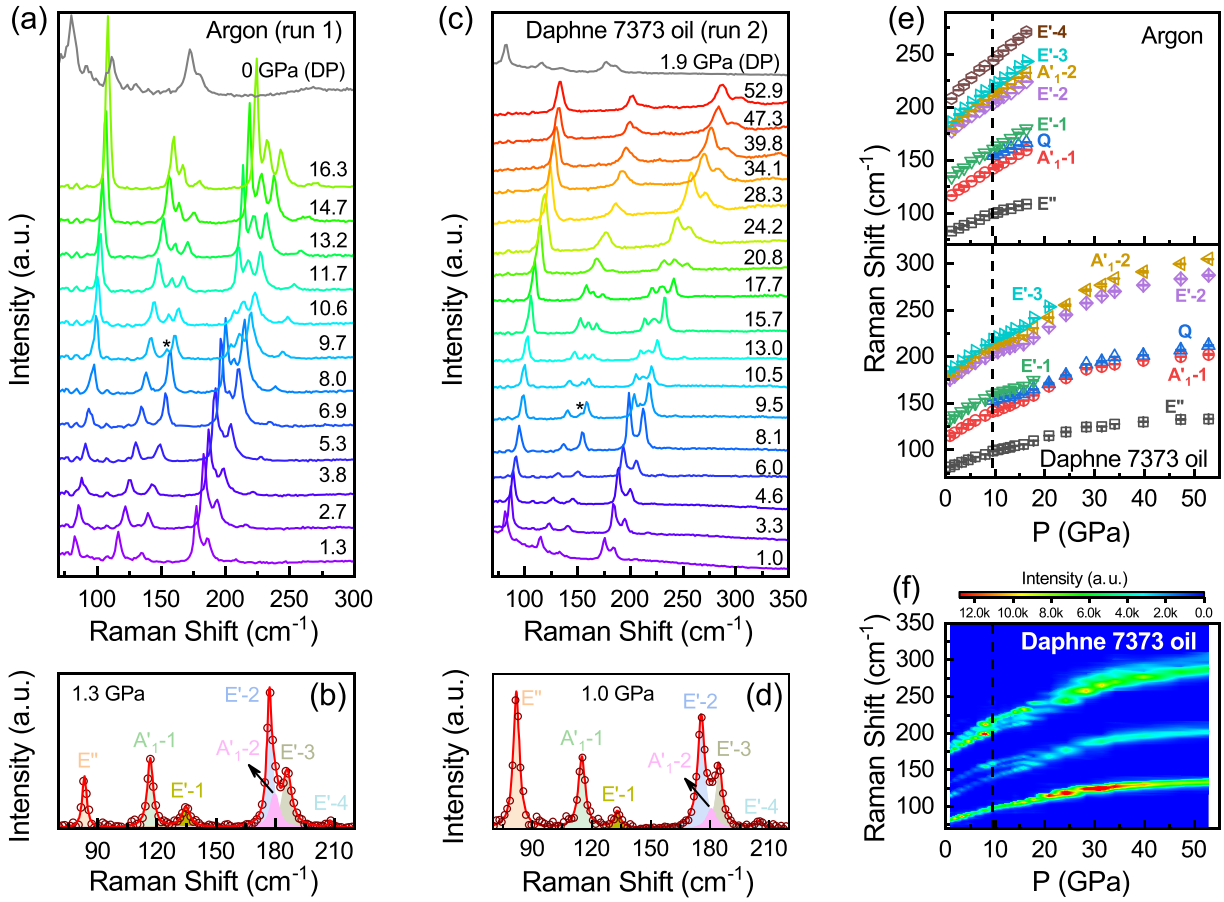

FIG. 5. Raman spectra of CaCdGe single crystal at various pressures using argon (a) and Daphne 7373 oil (c) as the pressure-transmitting medium, respectively. Upon compression, a new peak appears above ∼ 9.5 GPa, marked as a star. The Raman spectrum upon decompression back to the starting pressure is denoted by DP. (b),(d) Lorentzian line-shape fitting of Raman spectra at the initial compression pressure. Peak positions (e) and contour plot of Raman peaks (f) as a function of pressure. The vertical dashed lines represent the critical pressure.

of resistance exhibits a typical metallic conduction behavior, consistent with that at ambient pressure [6]. Upon compression to the highest pressure of 53.3 GPa, the metallic behavior is always observed. Nevertheless, above 13.7 GPa, the whole resistance curve shows an abrupt decrement [see Fig. 6(a)], which is consistent with the results in high-pressure Raman and XRD data. Here, the low-temperature resistance curves are fitted by using the power-law formula $R(T) = R_0 + A \times T^n$. The extracted exponent n and the temperature prefactor A coefficient as a function of pressure are displayed in Fig. 6(b). The inset of Fig. 6(b) shows a typical fitting of the $R(T)$ curve at 3.9 GPa. It can be seen that the value of n lies between 3 and 5 under high pressure, which indicates that the electron-phonon (*e-ph*) scattering dominates the low-temperature transport behavior [66]. In addition, with increasing pressure, n increases from the initial 3.5 to the maximum value of 4.9 around P_C, suggesting that the interband *s-d e-ph* scattering gradually transforms into the intraband *s-s e-ph* scattering [67]. However, n shows an abrupt decrement above P_C and returns back to 3 (i.e., original interband *s-d e-ph* scattering). In addition, the A coefficient also shows anomalous change across P_C. We noted that the high-temperature resistance curve (>100 K) exhibits a slight negative curvature ($d^2R/dT^2 < 0$). The similar behavior was also observed in Nb_3Sn [68] and has been described using a parallel-resistor model [69]: $\frac{1}{\rho(T)} = \frac{1}{\rho_1(T)} + \frac{1}{\rho_{sat}}$, where ρ_{sat} is the temperature-independent saturation resistivity and $\rho_1(T)$ is the ideal temperature-dependent resistivity dominated by *e-ph* scattering. $\rho_1(T) = \rho_0 + A(\frac{T}{\Theta_R})^5 \int_0^{\Theta_R/T} \frac{x^5 dx}{[\exp(x)-1][1-\exp(-x)]}$, where ρ_0 is residual resistivity, and the second term is the generalized Bloch-Grüneisen expression [70]. Figure 6(c) shows a typical fitting at 3.9 GPa by using a parallel-resistor model. The extracted Debye temperature (Θ_R) as a function of pressure is displayed in Fig. 6(d). Similar with pressure evolution of parameters A and n, a huge anomalous change of Θ_R is also observed across P_C, which implies the abnormal evolution of lattice vibration of CaCdGe. In addition, the residual resistance ratio $R_{300\,K}/R_{1.8\,K}$ and resistance at different temperatures as a function of pressure are presented in Figs. 6(e) and 6(f). Both of them show clear changes above 13.7 GPa (see vertical dashed lines), consistent with results from high-pressure XRD and Raman data. These abrupt changes in resistance further reflect on the occurrence of the isostructural transition across P_C.

IV. CONCLUSION

In summary, we have grown high quality of CaCdGe single crystal and systematically investigated its structural,

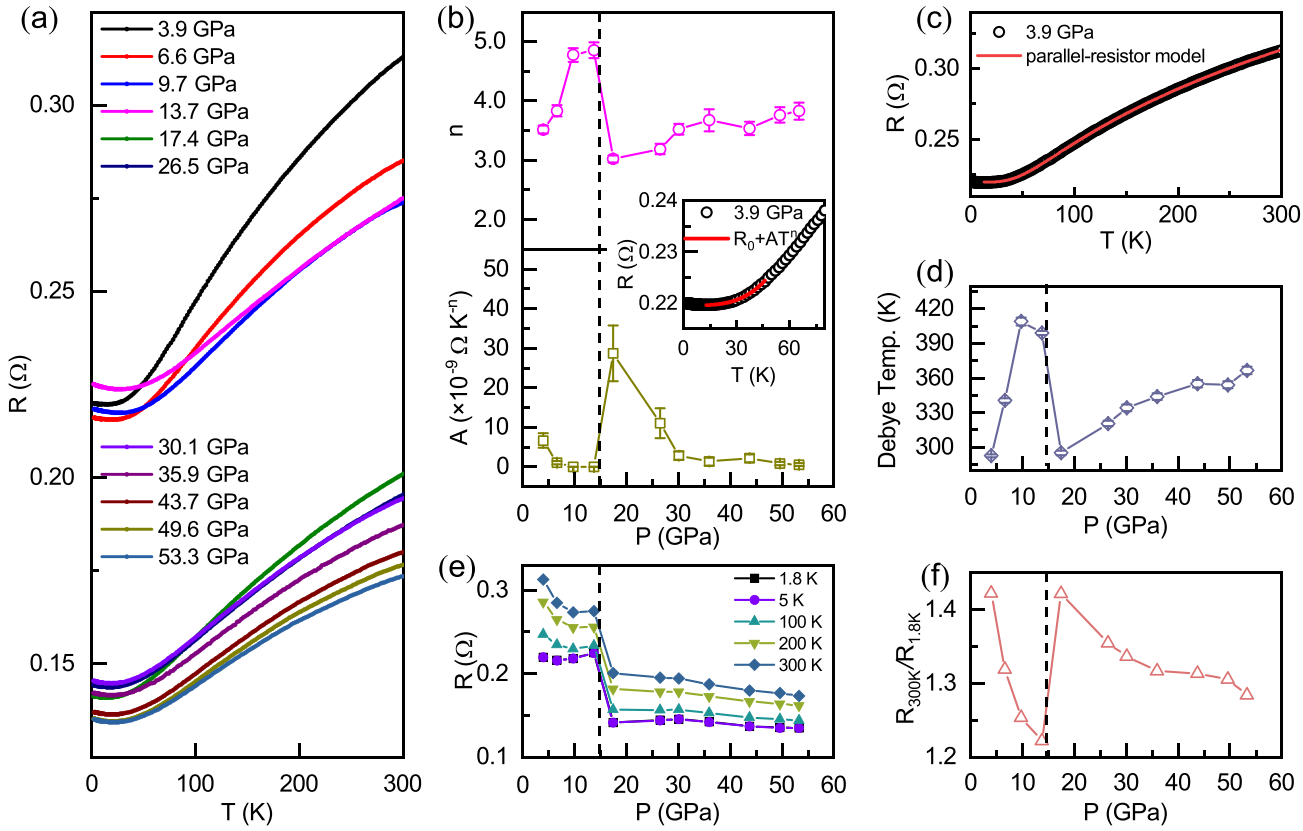

FIG. 6. (a) Temperature dependence of resistance under different pressures. (b) Pressure dependence of n and A from fitting of the low-temperature resistance by the power law $R(T) = R_0 + A \times T^n$. Error bars form fitting are within the symbols. The inset of (b) shows a typical fitting of R-T at 3.9 GPa by using the power law. (c) A typical fitting of R-T at 3.9 GPa by using the parallel-resistor model. (d) Pressure dependence of Debye temperature from fitting of the high-temperature resistance by the parallel-resistor model. (e) Pressure dependence of resistance at various temperatures. (f) $R_{300\,\mathrm{K}}/R_{1.8\,\mathrm{K}}$ as a function of pressure. The vertical dashed lines represent the critical pressure.

vibrational, and electrical transport properties under high pressure up to 53.3 GPa. Upon compression, although no evident structural transition is detected within 48.5 GPa, anomalies in lattice ratio c/a and bond angles are clearly observed around $P_C = 12.5$ GPa. Moreover, a new Raman peak Q appears across 9.5 GPa. Based on our high-pressure band structure calculations, the ETT is absent within 30.0 GPa. Combined with these abnormal features, we thus unveil a pressure-induced isostructural transition of CaCdGe at P_C, which is further supported by the abrupt change of resistance parameters (n, A, and Θ_R) through electrical transport measurements.

ACKNOWLEDGMENTS

We would like to thank Q. M. Zhang for constructive discussions and Z. M. Zhang for the technical support of gas loading in high-pressure Raman experiment. This work was financially supported by the National Key Research and Development Program of China (Grants No. 2022YFA1602603, No. 2021YFA1600204, and No. 2018YFA0305704), the National Natural Science Foundation of China (Grants No. 12004004, No. U19A2093, No. U1932152, No. 12174395, No. 12204004, and No. 12174397), the Key Project of Natural Scientific Research of Universities in Anhui Province (Grants No. KJ2021A0068 and No. KJ2021A0064), and the Users with Excellence Project of Hefei Center CAS (Grant No. 2021HSC-UE008). A portion of this work was supported by the High Magnetic Field Laboratory of Anhui Province under Contracts No. AHHM-FX-2020-02 and No. AHHM-FX-2021-03. Y.H.Z. was supported by the Youth Innovation Promotion Association CAS (Grant No. 2020443). The x-ray diffraction experiment was performed at the beamline BL15U1, Shanghai Synchrotron Radiation Facility.

[1] L. M. Schoop, M. N. Ali, C. Straßer, A. Topp, A. Varykhalov, D. Marchenko, V. Duppel, S. S. Parkin, B. V. Lotsch, and C. R. Ast, Dirac cone protected by non-symmorphic symmetry and three-dimensional Dirac line node in ZrSiS, Nat. Commun. **7**, 11696 (2016).

[2] J. Hu, Z. J. Tang, J. Y. Liu, X. Liu, Y. L. Zhu, D. Graf, K. Myhro, S. Tran, C. N. Lau, J. Wei, and Z. Q. Mao, Evidence of Topological Nodal-Line Fermions in ZrSiSe and ZrSiTe, Phys. Rev. Lett. **117**, 016602 (2016).

[3] B. J. Feng, B. T. Fu, S. Kasamatsu, S. Ito, P. Cheng, C.-C. Liu, Y. Feng, S. L. Wu, S. K. Mahatha, P. Sheverdyaeva, P. Moras, M. Arita, O. Sugino, T.-C. Chiang, K. Shimada, K. Miyamoto, T. Okuda, K. H. Wu, L. Chen, Y. G. Yao, and I. Matsuda, Experimental realization of two-dimensional Dirac

nodal line fermions in monolayer Cu_2Si, Nat. Commun. **8**, 1007 (2017).

[4] K. Kim, J. Seo, E. Lee, K.-T. Ko, B. S. Kim, B. G. Jang, J. M. Ok, J. Lee, Y. J. Jo, W. Kang, J. H. Shim, C. Kim, H. W. Yeom, B. I. Min, B.-J. Yang, and J. S. Kim, Large anomalous Hall current induced by topological nodal lines in a ferromagnetic van der Waals semimetal, Nat. Mater. **17**, 794 (2018).

[5] M. Hirayama, R. Okugawa, T. Miyake, and S. Murakami, Topological Dirac nodal lines and surface charges in fcc alkaline earth metals, Nat. Commun. **8**, 14022 (2017).

[6] E. Emmanouilidou, B. Shen, X. Y. Deng, T.-R. Chang, A. Shi, G. Kotliar, S.-Y. Xu, and N. Ni, Magnetotransport properties of the single-crystalline nodal-line semimetal candidates Ca*TX* (T = Ag, Cd; X = As, Ge), Phys. Rev. B **95**, 245113 (2017).

[7] A. Laha, S. Mardanya, B. Singh, H. Lin, A. Bansil, A. Agarwal, and Z. Hossain, Magnetotransport properties of the topological nodal-line semimetal CaCdSn, Phys. Rev. B **102**, 035164 (2020).

[8] G. Bian, T.-R. Chang, R. Sankar, S.-Y. Xu, H. Zheng, T. Neupert, C.-K. Chiu, S.-M. Huang, G. Q. Chang, I. Belopolski, D. S. Sanchez, M. Neupane, N. Alidoust, C. Liu, B. K. Wang, C.-C. Lee, H.-T. Jeng, C. L. Zhang, Z. J. Yuan, S. Jia *et al.*, Topological nodal-line fermions in spin-orbit metal $PbTaSe_2$, Nat. Commun. **7**, 10556 (2016).

[9] Q. N. Xu, R. Yu, Z. Fang, X. Dai, and H. M. Weng, Topological nodal line semimetals in the CaP_3 family of materials, Phys. Rev. B **95**, 045136 (2017).

[10] S. C. Li, Z. P. Guo, D. Z. Fu, X.-C. Pan, J. H. Wang, K. J. Ran, S. Bao, Z. Ma, Z. G. Cai, R. Wang, R. Yu, J. Sun, F. Q. Song, and J. S. Wen, Evidence for a Dirac nodal-line semimetal in $SrAs_3$, Sci. Bull. **63**, 535 (2018).

[11] W. Q. Zhou, A. N. Rudenko, and S. J. Yuan, Effect of mechanical strain on the optical properties of nodal-line semimetal ZrSiS, Adv. Electron. Mater. **6**, 1900860 (2019).

[12] C. Q. Xu, R. Sankar, W. Zhou, B. Li, Z. D. Han, B. Qian, J. H. Dai, H. B. Cui, A. F. Bangura, F. C. Chou, and X. F. Xu, Topological phase transition under pressure in the topological nodal-line superconductor $PbTaSe_2$, Phys. Rev. B **96**, 064528 (2017).

[13] D. VanGennep, T. A. Paul, C. W. Yerger, S. T. Weir, Y. K. Vohra, and J. J. Hamlin, Possible pressure-induced topological quantum phase transition in the nodal line semimetal ZrSiS, Phys. Rev. B **99**, 085204 (2019).

[14] M. Y. Qi, X. D. Zhu, Y. H. Zhou, C. An, C. H. Chen, Y. F. Yuan, B. W. Zhang, S. Y. Wang, Y. Zhou, X. L. Chen, R. R. Zhang, M. L. Tian, and Z. R. Yang, Emerging superconductivity and the origin of its enhancement in pressurized topological nodal-line semimetal $SrAs_3$, Adv. Electron. Mater. **6**, 2000293 (2020).

[15] E. Cheng, W. Xia, X. B. Shi, Z. H. Yu, L. Wang, L. M. Yan, D. C. Peets, C. C. Zhu, H. Su, Y. Zhang, D. Z. Dai, X. Wang, Z. Q. Zou, N. Yu, X. F. Kou, W. G. Yang, W. W. Zhao, Y. F. Guo, and S. Y. Li, Pressure-induced superconductivity and topological phase transitions in the topological nodal-line semimetal $SrAs_3$, npj Quantum Mater. **5**, 38 (2020).

[16] Y. Okamoto, K. Saigusa, T. Wada, Y. Yamakawa, A. Yamakage, T. Sasagawa, N. Katayama, H. Takatsu, H. Kageyama, and K. Takenaka, High-mobility carriers induced by chemical doping in the candidate nodal-line semimetal CaAgP, Phys. Rev. B **102**, 115101 (2020).

[17] Y. H. Kwan, P. Reiss, Y. Han, M. Bristow, D. Prabhakaran, D. Graf, A. McCollam, S. A. Parameswaran, and A. I. Coldea, Quantum oscillations probe the Fermi surface topology of the nodal-line semimetal CaAgAs, Phys. Rev. Res. **2**, 012055(R) (2020).

[18] H. T. Hirose, T. Terashima, T. Wada, Y. Matsushita, Y. Okamoto, K. Takenaka, and S. Uji, Real spin and pseudospin topologies in the noncentrosymmetric topological nodal-line semimetal CaAgAs, Phys. Rev. B **101**, 245104 (2020).

[19] N. Xu, Y. T. Qian, Q. S. Wu, G. Autès, C. E. Matt, B. Q. Lv, M. Y. Yao, V. N. Strocov, E. Pomjakushina, K. Conder, N. C. Plumb, M. Radovic, O. V. Yazyev, T. Qian, H. Ding, J. Mesot, and M. Shi, Trivial topological phase of CaAgP and the topological nodal-line transition in $CaAg(P_{1-x}As_x)$, Phys. Rev. B **97**, 161111(R) (2018).

[20] X.-B. Wang, X.-M. Ma, E. Emmanouilidou, B. Shen, C.-H. Hsu, C.-S. Zhou, Y. Zuo, R.-R. Song, S.-Y. Xu, G. Wang, L. Huang, N. Ni, and C. Liu, Topological surface electronic states in candidate nodal-line semimetal CaAgAs, Phys. Rev. B **96**, 161112(R) (2017).

[21] A. Yamakage, Y. Yamakawa, Y. Tanaka, and Y. Okamoto, Line-node dirac semimetal and topological insulating phase in noncentrosymmetric pnictides CaAgX (X = P, As), J. Phys. Soc. Jpn. **85**, 013708 (2016).

[22] Y. Okamoto, T. Inohara, A. Yamakage, Y. Yamakawa, and K. Takenaka, Low carrier density metal realized in candidate line-node Dirac semimetals CaAgP and CaAgAs, J. Phys. Soc. Jpn. **85**, 123701 (2016).

[23] D. Takane, K. Nakayama, S. Souma, T. Wada, Y. Okamoto, K. Takenaka, Y. Yamakawa, A. Yamakage, T. Mitsuhashi, K. Horiba, H. Kumigashira, T. Takahashi, and T. Sato, Observation of Dirac-like energy band and ring-torus Fermi surface associated with the nodal line in topological insulator CaAgAs, npj Quantum Mater. **3**, 1 (2018).

[24] J. Nayak, N. Kumar, S.-C. Wu, C. Shekhar, J. Fink, E. D. L. Rienks, G. H. Fecher, Y. Sun, and C. Felser, Electronic properties of topological insulator candidate CaAgAs, J. Phys.: Condens. Matter **30**, 045501 (2018).

[25] T. Hatano, I. Nakamura, S. Ohta, Y. Tomizawa, T. Urata, K. Iida, and H. Ikuta, Thin film growth of CaAgAs by molecular beam epitaxy, J. Phys.: Condens. Matter **32**, 435703 (2020).

[26] X. X. Xi, C. L. Ma, Z. X. Liu, Z. Q. Chen, W. Ku, H. Berger, C. Martin, D. B. Tanner, and G. L. Carr, Signatures of a Pressure-Induced Topological Quantum Phase Transition in BiTeI, Phys. Rev. Lett. **111**, 155701 (2013).

[27] Y. P. Qi, W. J. Shi, P. G. Naumov, N. Kumar, R. Sankar, W. Schnelle, C. Shekhar, F.-C. Chou, C. Felser, B. H. Yan, and S. A. Medvedev, Topological quantum phase transition and superconductivity induced by pressure in the bismuth tellurohalide BiTeI, Adv. Mater. **29**, 1605965 (2017).

[28] C. An, Y. H. Zhou, C. H. Chen, F. C. Fei, F. Q. Song, C. Y. Park, J. H. Zhou, H. G. Rubahn, V. V. Moshchalkov, X. L. Chen, G. F. Zhang, and Z. R. Yang, Long-range ordered amorphous atomic chains as building blocks of a superconducting quasi-one-dimensional crystal, Adv. Mater. **32**, 2002352 (2020).

[29] L.-L. Zhang, S. Yan, S. Jiang, K. Yang, H. Wang, S.-M. He, D.-X. Liang, L. Zhang, Y. He, X.-Y. Lan, C.-W. Mao, J. Wang, H. Jiang, Y. Zheng, Z.-H. Dong, L.-Y. Zeng, and A.-G. Li, Hard x-ray micro-focusing beamline at SSRF, Nucl. Sci. Tech. **26**, 060101 (2015).

[30] C. Prescher and V. B. Prakapenka, *DIOPTAS*: A program for reduction of two-dimensional X-ray diffraction data and data exploration, High Press. Res. **35**, 223 (2015).

[31] B. H. Toby, EXPGUI, a graphical user interface for GSAS, J. Appl. Crystallogr. **34**, 210 (2001).

[32] K. Syassen, Ruby under pressure, High Press. Res. **28**, 75 (2008).

[33] A. Togo and I. Tanaka, First principles phonon calculations in materials science, Scr. Mater. **108**, 1 (2015).

[34] G. Kresse and J. Hafner, *Ab initio* molecular dynamics for liquid metals, Phys. Rev. B **47**, 558 (1993).

[35] G. Kresse and J. Furthmüller, Efficient iterative schemes for *ab initio* total-energy calculations using a plane-wave basis set, Phys. Rev. B **54**, 11169 (1996).

[36] J. P. Perdew, K. Burke, and M. Ernzerhof, Generalized Gradient Approximation Made Simple, Phys. Rev. Lett. **77**, 3865 (1996).

[37] G. Kresse and D. Joubert, From ultrasoft pseudopotentials to the projector augmented-wave method, Phys. Rev. B **59**, 1758 (1999).

[38] P. E. Blochl, Projector augmented-wave method, Phys. Rev. B **50**, 17953 (1994).

[39] F. Tran and P. Blaha, Accurate Band Gaps of Semiconductors and Insulators with a Semilocal Exchange-Correlation Potential, Phys. Rev. Lett. **102**, 226401 (2009).

[40] F. Birch, Finite elastic strain of cubic crystals, Phys. Rev. **71**, 809 (1947).

[41] P. F. Shen, X. Ma, Z. Guan, Q. J. Li, H. F. Zhang, R. Liu, B. Liu, X. G. Yang, Q. Dong, T. Cui, and B. B. Liu, Linear tunability of the band gap and two-dimensional (2D) to three-dimensional (3D) isostructural transition in WSe_2 under high pressure, J. Phys. Chem. C **121**, 26019 (2017).

[42] K. K. Pandey, H. K. Poswal, R. Kumar, and S. M. Sharma, High pressure iso-structural phase transition in $BiMn_2O_5$, J. Phys.: Condens. Matter **25**, 325401 (2013).

[43] I. Efthimiopoulos, J. Kemichick, X. Zhou, S. V. Khare, D. Ikuta, and Y. J. Wang, High-pressure studies of Bi_2S_3, J. Phys. Chem. A **118**, 1713 (2014).

[44] V. Rajaji, U. Dutta, P. C. Sreeparvathy, S. C. Sarma, Y. A. Sorb, B. Joseph, S. Sahoo, S. C. Peter, V. Kanchana, and C. Narayana, Structural, vibrational, and electrical properties of $1T-TiTe_2$ under hydrostatic pressure: Experiments and theory, Phys. Rev. B **97**, 085107 (2018).

[45] C. Raptis, R. L. McGreevy, and D. G. Seguier, Temperature-induced structural phase transition in $CaBr_2$ studied by Raman spectroscopy, Phys. Rev. B **39**, 7996 (1989).

[46] S. Saha, D. V. S. Muthu, C. Pascanut, N. Dragoe, R. Suryanarayanan, G. Dhalenne, A. Revcolevschi, S. Karmakar, S. M. Sharma, and A. K. Sood, High-pressure Raman and x-ray study of the spin-frustrated pyrochlore $Gd_2Ti_2O_7$, Phys. Rev. B **74**, 064109 (2006).

[47] See Supplemental Material at http://link.aps.org/supplemental/10.1103/PhysRevB.108.014109 for additional (fitting results of Raman spectra, FWHM, and band structure calculations) information.

[48] S. Klotz, J.-C. Chervin, P. Munsch, and G. Le Marchand, Hydrostatic limits of 11 pressure transmitting media, J. Phys. D: Appl. Phys. **42**, 075413 (2009).

[49] A. Nakayama, K. Aoki, and R. P. Carlón, Raman study of pressure-induced structural change in C_6I_6 up to 47 GPa, Phys. Rev. B **64**, 064104 (2001).

[50] D. Errandonea, F. J. Manjón, N. Garro, P. Rodríguez-Hernández, S. Radescu, A. Mujica, A. Muñoz, and C. Y. Tu, Combined Raman scattering and *ab initio* investigation of pressure-induced structural phase transitions in the scintillator $ZnWO_4$, Phys. Rev. B **78**, 054116 (2008).

[51] D. V. S. Muthu, P. Teredesai, S. Saha, U. V. Waghmare Suchitra, A. K. Sood, and C. N. R. Rao, Pressure-induced structural phase transitions and phonon anomalies in ReO_3: Raman and first-principles study, Phys. Rev. B **91**, 224308 (2015).

[52] S. Pal, R. Arora, S. Roychowdhury, L. Harnagea, K. Saurabh, S. Shenoy, D. V. S. Muthu, K. Biswas, U. V. Waghmare, and A. K. Sood, Pressure-induced phase transitions in the topological crystalline insulator SnTe and its comparison with semiconducting SnSe: Raman and first-principles studies, Phys. Rev. B **101**, 155202 (2020).

[53] A. L. J. Pereira, L. Gracia, D. Santamaría-Pérez, R. Vilaplana, F. J. Manjón, D. Errandonea, M. Nalin, and A. Beltrán, Structural and vibrational study of cubic Sb_2O_3 under high pressure, Phys. Rev. B **85**, 174108 (2012).

[54] L. R. Wang, K. Wang, G. J. Xiao, Q. S. Zeng, and B. Zou, Pressure-induced structural evolution and band gap shifts of organometal halide perovskite-based methylammonium lead chloride, J. Phys. Chem. Lett. **7**, 5273 (2016).

[55] Y. S. Zhao, W. G. Yang, N. N. Li, Y. Li, R. L. Tang, H. Li, H. Y. Zhu, P. W. Zhu, and X. Wang, Pressure-enhanced insulating state and trigonal distortion relaxation in geometrically frustrated pyrochlore $Eu_2Sn_2O_7$, J. Phys. Chem. C **120**, 9436 (2016).

[56] L. Zhang, Q. X. Zeng, and K. Wang, Pressure-induced structural and optical properties of inorganic halide perovskite $CsPbBr_3$, J. Phys. Chem. Lett. **8**, 3752 (2017).

[57] I. M. Lifshitz, Anomalies of electron characteristics of a metal in the high pressure region, Sov. Phys. JETP **11**, 1130 (1960).

[58] Y. Zhou, C. An, X. L. Chen, Y. H. Zhou, Y. Fang, Z. T. Zhang, and Z. R. Yang, Pressure evolution of electronic and structural properties in transition metal dichalcogenide $1T-Co_{1.06}Te_2$, J. Phys.: Condens. Matter **34**, 315704 (2022).

[59] R. Vilaplana, D. Santamaría-Pérez, O. Gomis, F. J. Manjón, J. González, A. Segura, A. Muñoz, P. Rodríguez-Hernández, E. Pérez-González, V. Marín-Borrás, V. Muñoz-Sanjose, C. Drasar, and V. Kucek, Structural and vibrational study of Bi_2Se_3 under high pressure, Phys. Rev. B **84**, 184110 (2011).

[60] M. Krottenmüller, M. Vöst, N. Unglert, J. Ebad-Allah, G. Eickerling, D. Volkmer, J. Hu, Y. L. Zhu, Z. Q. Mao, W. Scherer, and C. A. Kuntscher, Indications for Lifshitz transitions in the nodal-line semimetal ZrSiTe induced by interlayer interaction, Phys. Rev. B **101**, 081108(R) (2020).

[61] A. Bera, K. Pal, D. V. S. Muthu, S. Sen, P. Guptasarma, U. V. Waghmare, and A. K. Sood, Sharp Raman Anomalies and Broken Adiabaticity at a Pressure Induced Transition from Band to Topological Insulator in Sb_2Se_3, Phys. Rev. Lett. **110**, 107401 (2013).

[62] A. Polian, M. Gauthier, S. M. Souza, D. M. Trichês, J. C. de Lima, and T. A. Grandi, Two-dimensional pressure-induced electronic topological transition in Bi_2Te_3, Phys. Rev. B **83**, 113106 (2011).

[63] R. Vilaplana, O. Gomis, F. J. Manjón, A. Segura, E. Pérez-González, P. Rodríguez-Hernández, A. Muñoz, J. González, V. Marín-Borrás, V. Muñoz-Sanjosé, C. Drasar, and V. Kucek,

High-pressure vibrational and optical study of Bi_2Te_3, Phys. Rev. B **84**, 104112 (2011).

[64] O. Gomis, R. Vilaplana, F. J. Manjón, P. Rodríguez-Hernández, E. Pérez-González, A. Muñoz, V. Kucek, and C. Drasar, Lattice dynamics of Sb_2Te_3 at high pressures, Phys. Rev. B **84**, 174305 (2011).

[65] G. K. Pradhan, A. Bera, P. Kumar, D. V. S. Muthu, and A. K. Sood, Raman signatures of pressure induced electronic topological and structural transitions in Bi_2Te_3, Solid State Commun. **152**, 284 (2012).

[66] F. Nava, E. Mazzega, M. Michelini, O. Laborde, O. Thomas, J. P. Senateur, and R. Madar, Analysis of the electrical resistivity of Ti, Mo, Ta, and W monocrystalline disilicides, J. Appl. Phys. **65**, 1584 (1989).

[67] X. Zhang, Z. W. Xiao, H. C. Lei, Y. Toda, S. Matsuishi, T. Kamiya, S. Ueda, and H. Hosono, Two-dimensional transition-metal electride Y_2C, Chem. Mater. **26**, 6638 (2014).

[68] Z. Fisk and G. W. Webb, Saturation of the High-Temperature Normal-State Electrical Resistivity of Superconductors, Phys. Rev. Lett. **36**, 1084 (1976).

[69] H. Wiesmann, M. Gurvitch, H. Lutz, A. Ghosh, B. Schwarz, M. Strongin, P. B. Allen, and J. W. Halley, Simple Model for Characterizing the Electrical Resistivity in *A*-15 Superconductors, Phys. Rev. Lett. **38**, 782 (1977).

[70] B. J. Lv, M. C. Li, J. Chen, Y. S. Yang, S. Q. Wu, L. Qiao, F. H. Guan, H. Xing, Q. Tao, G.-H. Cao, and Z.-A. Xu, Type-I superconductivity in noncentrosymmetric $NbGe_2$, Phys. Rev. B **102**, 064507 (2020).